Fourier-transform infrared spectroscopy with undetected photons from high-gain spontaneous parametric down-conversion

Check for updates

Kazuki Hashimoto [1]✉, Dmitri B. Horoshko [2], Mikhail I. Kolobov[2], Yoad Michael[3], Ziv Gefen[3] & Maria V. Chekhova [1,4]

Fourier-transform infrared spectroscopy (FTIR) is an indispensable analytical method that allows label-free identification of substances via fundamental molecular vibrations. However, traditional FTIR spectrometers require mid-infrared (MIR) elements, including low-efficiency MIR photodetectors. SU(1,1) interferometry has previously enabled FTIR with undetected MIR photons via spontaneous parametric down-conversion in the low-parametric-gain regime, where the number of photons per mode is much less than one and sensitive photodetectors are needed. In this work, we develop a high-parametric-gain SU(1,1) interferometer for MIR-range FTIR with undetected photons. Using our method, we demonstrate three major advantages: a high photon number at the interferometer output, a considerably lower photon number at the sample, and improved interference contrast. In addition, we broaden the spectral range of the interferometer by aperiodic poling in the gain medium. Exploiting the broadband SU(1,1) interferometer, we measure and evaluate the MIR absorption spectra of polymers in the 3-μm region.

Fourier-transform infrared spectroscopy (FTIR) is used in various applications such as environmental gas sensing[1] or medical diagnosis[2] as an analytical tool that allows label-free measurements of samples via fundamental molecular vibrations. It obtains broadband mid-infrared (MIR) spectra via time-domain linear interferograms measured with a Michelson interferometer illuminated by a thermal source (e.g., Globar)[3]. However, conventional FTIR spectrometers need MIR optical components, including low-sensitivity MIR photodetectors. To get around this difficulty, recently developed upconversion schemes use visible/near-IR photodetectors for detection. Some research groups have developed upconversion MIR spectroscopy with nonlinear frequency conversion[4–8] or field-resolved spectroscopy with electro-optic sampling[9,10]. However, these methods often require broadband MIR pulsed lasers (and pump sources to generate the MIR pulses), dispersion compensation schemes, and/or other high-power lasers for frequency conversion, which makes the spectroscopy system complex. Another approach is the photon-pair coincidence measurement with an upconversion scheme[11,12], but it requires a highly sensitive photodetector working in the photon counting regime, which fundamentally restricts the spectral acquisition speed.

SU(1,1) interferometry[13] with a narrowband pump source has been recently applied to FTIR as a simple approach to measuring MIR spectra without directly detecting MIR photons. In this technique, nondegenerate spontaneous parametric down-conversion (SPDC) in a nonlinear crystal is used to generate correlated pairs of signal (e.g., visible) and idler (e.g., MIR) photons. A second SPDC process then occurs sequentially, forming a nonlinear interferometer. The absorption of idler photons between the two crystals affects the signal interference at the interferometer output, which enables measuring the idler absorption without detecting the idler photons ('spectroscopy with undetected photons')[14–21]. FTIR with undetected photons has been implemented with SPDC in the low-parametric-gain regime[15,16,18,20,21], where the number of photons per mode is much less than one, and relatively sensitive detectors are needed at the output.

Alternatively, if the SU(1,1) interferometer operates under a high parametric gain[22–25], exploiting an intense pulsed laser as a pump source, photon pairs generated by the first crystal seed parametric down-conversion (PDC) in the second one. This high-gain version of spectroscopy with 'undetected photons' has several major advantages. First, it results in higher output powers, sufficient even for a photodetector with moderate sensitivity.

[1]Max Planck Institute for the Science of Light, Staudtstr. 2, 91058 Erlangen, Germany. [2]Univ. Lille, CNRS, UMR 8523 - PhLAM - Physique des Lasers Atomes et Molécules, F-59000 Lille, France. [3]Raicol Crystals, Hamelacha 22, 4809162 Rosh Ha'Ayin, Israel. [4]Friedrich-Alexander-Universität Erlangen-Nürnberg, Staudtstr. 7/B2, 91058 Erlangen, Germany. ✉e-mail: kazuki.hashimoto@mpl.mpg.de

Second, due to the amplification in the second crystal, the MIR beam on the sample can be weak enough to interrogate the sample non-invasively. Finally, the interference visibility has a nonlinear dependence on idler amplitude transmittance and can be high even under strong absorption. After demonstrating Fourier-transform near-infrared spectroscopy with undetected photons using a high-parametric-gain SU(1,1) interferometer[26], we are now extending the wavelength region to MIR and evaluating the system in this region, which is a significant step for the FTIR spectrometer.

Here, we demonstrate MIR-range FTIR with undetected photons exploiting a high-parametric-gain SU(1,1) interferometer. First, we characterize the bright twin beams (signal: ~0.6 μm, idler: ~3 μm) generated via high-parametric-gain SPDC in periodically and aperiodically poled potassium titanyl phosphate crystals (ppKTP and apKTP, respectively). In addition, we measure and evaluate the signal interferogram generated from the interferometer to show the characteristics of the high-parametric-gain SU(1,1) interferometer. Using the developed FTIR spectrometer, we measure broadband MIR spectra of polymer films within a spectral bandwidth of ~300 cm^{-1}, assign some MIR absorption peaks that appear in the spectra, and evaluate the sensitivity.

Results
Experimental setup
We develop a high-parametric-gain SU(1,1) interferometer to demonstrate FTIR with undetected photons (Fig. 1). A 532-nm 15-ps pulsed laser with a repetition rate of 1 kHz (PL2210A-1K-SH/TH, Ekspla) is focused into a $\chi^{(2)}$ nonlinear crystal using an $f = 200$ mm lens. The pump polarization is adjusted with a half-wave plate. We use ppKTP or apKTP (Raicol Crystals) as the nonlinear crystal. Both crystals are 10-mm long and designed for type-0 phase matching. The poling period of the ppKTP crystal is fixed at 13.3 μm, and that of apKTP gradually increases from 12.3 to 14.0 μm along the crystal. The detailed design of the apKTP crystal is presented in Supplementary Note 3. The crystal temperature is adjusted with an oven. The high-parametric-gain SPDC inside a nonlinear crystal generates bright twin beams (signal: visible, idler: MIR).

The signal and pump pulses, reflected by a dichroic mirror (DM), travel through the reference arm and return to the same path after being reflected by an $f = 100$ mm spherical mirror. The idler pulse goes to the scan arm and is collimated with an $f = 100$ mm CaF$_2$ lens. The collimated idler pulse passes through the test sample, is reflected by an end mirror, and travels back to the same path. The end mirror is placed on a motorized stage for scanning the optical path-length difference (OPD) between the reference and scan arms. The three pulses are again focused into the nonlinear crystal for a second PDC process. Inside the crystal, the signal pulse is amplified or de-amplified depending on the pump phase relative to the sum of signal and idler phases introduced by the motorized stage. The resultant signal interferogram contains information on the idler absorption because the absorption changes the number of amplified signal photons. After the crystal, the signal pulse is separated from the pump pulse with a DM and collimated with an $f = 100$ mm lens. The residual pump after the DM is

removed by long-pass filters. The collimated signal pulse is detected with a Si power meter (S130VC, Thorlabs) with 15-Hz radio-frequency (RF) low-pass filtering. The velocity of the motorized stage v is set to 6–18 μm s^{-1}, corresponding to the down-conversion factor ($= 2v/c$, where c denotes the speed of light) of 0.4×10^{-13}–1.2×10^{-13}. The upper velocity is limited by the cut-off frequency of the RF low-pass filter (15 Hz). By implementing an RF low-pass filter with a higher cut-off frequency, the stage speed can be improved more until the highest frequency of the RF spectrum reaches the Nyquist frequency (500 Hz). The measured signal interferogram is digitized and post-processed to obtain the FTIR spectrum (see Methods).

Spontaneous parametric down-conversion spectra
First, we evaluate the signal spectrum generated by the SPDC process inside the ppKTP crystal. Figure 2a shows the signal spectra measured with a visible spectrometer (AvaSpec-ULS3648-USB2, Avantes) with a spectral resolution of 1.4 nm at several crystal temperatures from 25 to 195 °C. The central wavelength of the signal spectrum changes from 637 nm (15,700 cm^{-1}) to 626 nm (15,970 cm^{-1}) with temperature tuning. The intensity drop at shorter wavelengths is due to the idler absorption originating from the second overtone bands of the fundamental vibrations of KTP[27]. The idler absorption inside the crystal reduces the number of signal photons generated by high-parametric-gain SPDC. We also measure the average signal power dependence on the pump power at a crystal temperature of 22 °C (Fig. 2b). The number of photons per mode generated by the SPDC process is theoretically described as $N = \sinh^2 r$, where r denotes the parametric gain, being proportional to the square root of the pump power. The signal power exponentially increases with the pump power and saturates above ~400 μW. We attribute the saturation behavior to the pump depletion due to the efficient generation of signal and idler photons[28]. The signal power obtained at a pump power of 400 μW is around 8 μW. The unsaturated data are fitted with the function $y = A\sinh^2(B\sqrt{x})$, where $A = 5.1 \times 10^{-19}$ and $B = 25$ are the fitting coefficients. Considering the fitting curve, we achieve $r{\sim}16$ at a pump power of 400 μW. Note that the signal spatiotemporal structure should be single-mode when strictly measuring the parametric gain, but here, we check it without the mode selection. We also evaluate spectral-bandwidth broadening with a temperature gradient inside the ppKTP crystal in Supplementary Note 6.

Next, we measure the broadband signal spectrum generated from the apKTP crystal at ambient temperature. In this measurement, we use $f = 300$ mm lens to focus the pump pulse into the crystal. Figure 2c compares the measured and the simulated signal spectra. The simulated spectrum is obtained by convolving the spectrum calculated with the Rosenbluth parameter[29,30] of 0.6 with a 1.4-nm-width Gaussian function to match the spectral resolution. The measured bandwidth of 900 cm^{-1} (from 15,170 to 16,070 cm^{-1}) agrees well with the simulated one (920 cm^{-1}). The spectral bandwidth decreases by increasing the pump power because the signal spectrum is non-uniformly amplified. The spectral components generated near the output of the crystal grow faster than the beginning (see Supplementary Note 4). We attribute the spectral narrowing to the nonlinear

---

Fig. 1 | Schematic of the SU(1,1) interferometer for FTIR with undetected photons. HWP half-wave plate, DM dichroic mirror, M mirror, LPFs long-pass filters, PD photodetector. Either ppKTP or apKTP is used as the nonlinear crystal for the interferometer. The inset shows a signal interferogram generated by the ppKTP crystal without any sample, which is measured with the Si power meter and recorded with the software for the console (PM100D, Thorlabs).
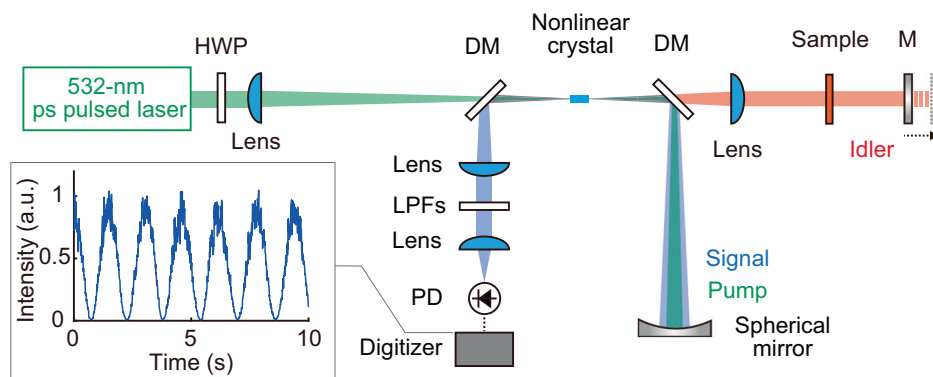
Fig. 2 | Evaluation of signal spectra. a Signal spectra generated by the first SPDC process in the ppKTP crystal for several crystal temperatures. The spectrum is tunable over 270 cm^{-1}-width by controlling the temperature. **b** Signal power vs. pump power. The blue points are the measurements, and the sky-blue line is the curve fitting the first 10 data points. The fitting function is $y = A\sinh^2(B\sqrt{x})$, with $A = 5.1 \times 10^{-19}$ and $B = 25$ being the fitting parameters. The X- and Y-error bars indicate the standard deviation of the pump and signal powers, respectively. **c** Measured (solid blue) and simulated (dotted sky-blue) signal spectra generated from the apKTP crystal at ambient temperature.
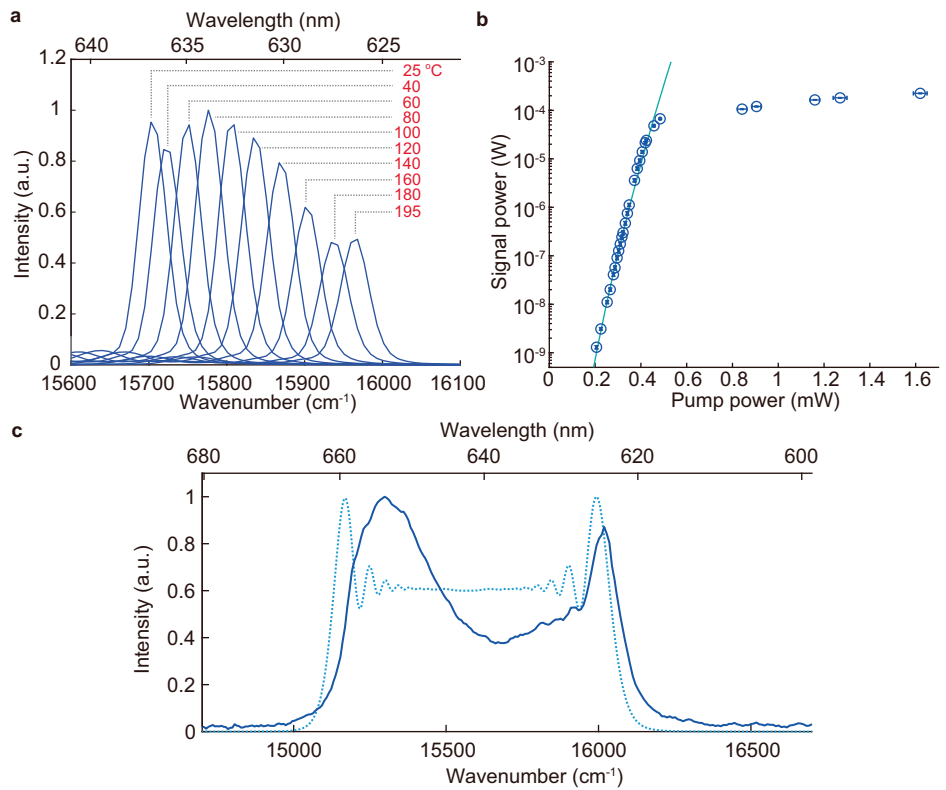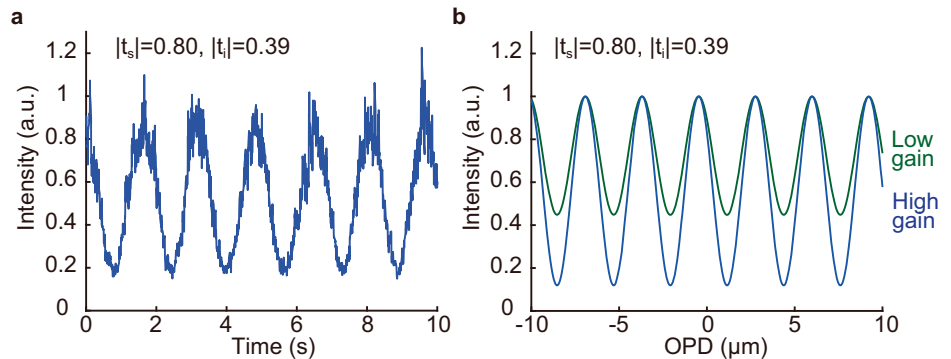

Fig. 3 | Visibility evaluation. a A signal interferogram measured at an idler amplitude transmittance $|t_i| = 0.39$ and a signal amplitude transmittance $|t_s| = 0.80$. The visibility is 67%. **b** Simulated signal interferograms at $|t_i| = 0.39$ and $|t_s| = 0.80$ with a parametric gain of 11 (blue) and 0.1 (green). The visibilities at the high- and low-parametric-gain regimes are 79% and 38%, respectively. Each interferogram is normalized to the peak intensity. OPD optical path-length differences.

conversion, such as sum-frequency generation, of the generated signal photons during the propagation. In addition, the sidebands are observed at 580–620 nm and around 550 nm, which are discussed in Supplementary Note 4.

Visibility evaluation

We measure the signal interferogram using the SU(1,1) interferometer with the ppKTP crystal and characterize the visibility. The interferograms are measured with the power meter and recorded with the software for the power meter console. Figure 3a shows the signal interferogram measured at (double-pass) idler and signal amplitude transmittances of $|t_i| = 0.39$ and $|t_s| = 0.80$, respectively, with a visibility of 67%. The visibility is evaluated as $V = (J_{max} - J_{max})/(J_{max} + J_{max})$, where J_{max} and J_{min} denote the maximum and minimum intensities of the interferograms after eliminating the high-frequency noises by smoothing. Meanwhile, the same transmittances would lead to much lower visibility if the interference were measured at a low parametric gain. Figure 3b shows the simulated interferograms[23] at $|t_i| = 0.39$ and $|t_s| = 0.80$ with a parametric gain of 11 (high-parametric-

gain regime) and 0.1 (low-parametric-gain regime). The high-gain simulated interferogram has visibility close to the experimental one (79%), but the low-gain visibility is much lower (38%). This is because, while the visibility in the low-parametric-gain regime is linear in $|t_i|$, $V_L = \frac{2|t_s|}{1+|t_s|^2}|t_i|$, the visibility in the high-parametric-gain regime is nonlinear in $|t_i|$, $V_H = \frac{2|t_s|}{|t_i|^2+|t_s|^2}|t_i|$. Note that the former equation is derived under the approximation that the parametric gain is significantly lower than 1 and equal for the first and second PDC processes, while the latter is derived under the approximation that the gain is significantly higher than 1.

FTIR interferograms and spectra

Figure 4a, b shows the FTIR interferograms (AC-coupled interferograms) measured with the ppKTP and apKTP crystals, respectively, with a maximum OPD of 1.6 mm. The former is a single-shot interferogram at a crystal temperature of 21 °C and a measurement time of 133 s, and the latter is a 36-times-averaged one at a crystal temperature of 150 °C and a total measurement time of 1581 s (corresponding to a single-shot measurement time

Fig. 4 | FTIR interferograms and spectra. a, b FTIR interferograms obtained with the ppKTP and apKTP crystals, respectively. The inset shows the zoomed view of the interferogram shown in (**a**). OPD optical path-length differences, ppKTP and apKTP periodically and aperiodically poled potassium titanyl phosphate, respectively. **c, d** FTIR spectra obtained by Fourier-transforming the interferograms shown in (**a**) and (**b**), respectively.
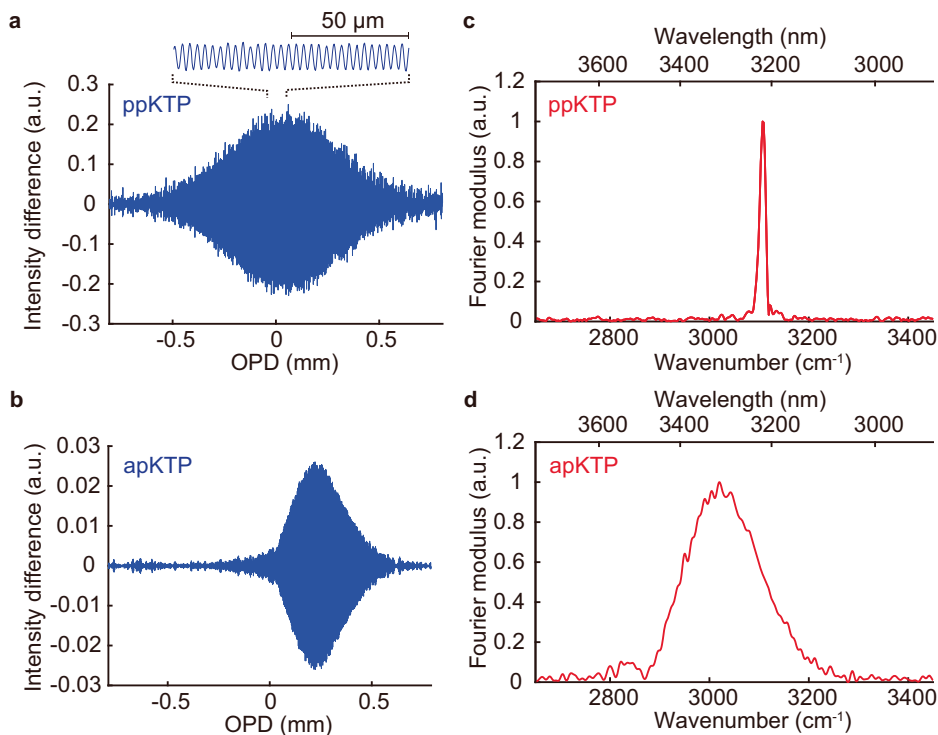
of 44 s). The apKTP crystal is heated to mitigate the signal-intensity decrease that occurred at room temperature with high pump power. We attribute the intensity decrease to the gray tracking effects inside the KTP crystal[31,32].

Figure 4c, d shows the FTIR spectra obtained by Fourier-transforming the interferograms shown in Fig. 4a, b, respectively. The spectral resolution is limited either by the maximum OPD or the pump coherence length[33], and the former dominates the resolution in our measurement. We define the resolution as the full-width at half-maximum (FWHM) of the sinc function (5 cm^{-1}) obtained by Fourier transforming the unapodized FTIR interferogram whose OPD from the center burst to one end is 1 mm (due to the asymmetricity of the measured interferogram). In the ppKTP crystal case, the FWHM width of the FTIR spectrum is 14 cm^{-1}. The Fourier modulus exponentially increases as the pump power increases and saturates at a pump power of ~250 μW (see Supplementary Note 2). At a pump power of 210 μW, the mean power of the signal detected with the Si power meter is 580 nW (580 pJ), while the idler power at the sample is expected to be around only 0.2 nW (0.2 pJ). The wavenumber (wavelength) varies from 3109 cm^{-1} (3216 nm) to 2855 cm^{-1} (3503 nm) by tuning the temperature from 21 to 190 °C. In the apKTP crystal case, the spectral bandwidth of the FTIR spectrum evaluated at −10-dB Fourier-modulus level is 300 cm^{-1} (the FWHM bandwidth is 170 cm^{-1}). The spectral narrowing discussed in the SPDC generation in the first passage also appears in the signal spectrum after the second passage, decreasing the FTIR bandwidth. The mean power detected with the power meter is around 10 nW (10 pJ) at a pump power of 1.37 mW.

MIR spectroscopy

Finally, we measure the MIR transmittance spectra of polymer films with the developed system. Figure 5a, b shows the (intensity) transmittance spectra of a polystyrene film and a plastic wrap, respectively, measured with the SU(1,1) interferometer (red points) with the ppKTP crystal and the reference spectra measured with a standard FTIR spectrometer (Varian 670-IR, Varian) (dotted gray lines) with a spectral resolution of 16 cm^{-1}. The Fourier modulus measured with the SU(1,1) interferometer is proportional to the double-pass idler amplitude transmittance, which is equal to the intensity transmittance, entering Eq. (S2) in Supplementary Note 1. To obtain the transmittance, we integrate the Fourier moduli of the FTIR spectra (with and without the samples) over a bandwidth of 17 cm^{-1}. The MIR transmittance spectra measured with our method agree well with the reference spectra. We observe fundamental molecular vibrations of polystyrene in the measured IR spectrum, for example, CH$_2$ asymmetric stretching at 2923 cm^{-1} and aromatic CH stretchings at 3016 cm^{-1} and 3057 cm^{-1} [34]. Also, we observe large absorption bands in the plastic-wrap spectrum and attribute them to C–H stretching modes.

Figure 5c shows the 36-times averaged FTIR spectra with and without the sample measured with the apKTP crystal. The spectrum taken with the sample contains several absorption peaks originating from the molecular vibrations of polystyrene. Figure 5d shows the MIR (intensity) transmittance spectra of a polystyrene film measured with the SU(1,1) interferometer (solid red) and the reference spectra (dotted gray) with a spectral resolution of 5 cm^{-1}. We clearly obtain the absorption lines of polystyrene. The transmittance mismatch between our method and the standard FTIR spectrometer could be due to the surface quality of the sample. The sample's surface roughness may affect the spatial-mode profile of the idler beam, degrading the SU(1,1) interference compared to the no-sample case. If it is the cause, the solution would be to focus the idler beam onto the sample with additional lenses or to exploit a camera for detection to monitor the beam profile distortion.

Discussion

The spectral range of the signal generated by the first SPDC process from the 10-mm ppKTP crystal with the temperature control is 270 cm^{-1}, and that of the 10-mm apKTP crystal is more than three times broader (900 cm^{-1}). Increasing/decreasing the temperature (e.g., to above 200 °C and/or below 10 °C) of the ppKTP crystal leads to expanding the spectral range in principle. In the apKTP crystal case, the spectral bandwidth of the FTIR spectrum obtained with the apKTP crystal is 300 cm^{-1}, which is only one-third of the spectral bandwidth generated via the first SPDC process. This reduction is caused by the frequency upconversion of the signal photons at the beginning of the crystal (see Supplementary Note 4). We assume the optimization of the chirp function can improve the bandwidth of the signal spectrum at the interferometer output.

Fig. 5 | MIR spectroscopy of polymers. a, b MIR (intensity) transmittance spectra of a polystyrene film and a plastic wrap, respectively, measured with the ppKTP crystal using the temperature tuning scheme. The red points are measured with the SU(1,1) interferometer and the dotted gray lines, with a standard FTIR spectrometer with a spectral resolution of 16 cm^{-1}. The solid and dotted arrows show the aromatic CH stretching and CH$_2$ asymmetric stretching modes, respectively. **c** FTIR spectra obtained with the apKTP crystal. The red line represents the spectrum with a polystyrene film, and the orange line represents the one without the sample. **d** MIR (intensity) transmittance spectra of a polystyrene film. The solid-red and dotted-gray lines show the transmittance spectra measured with our system (with the apKTP crystal) and a standard FTIR spectrometer with a spectral resolution of 5 cm^{-1}, respectively.
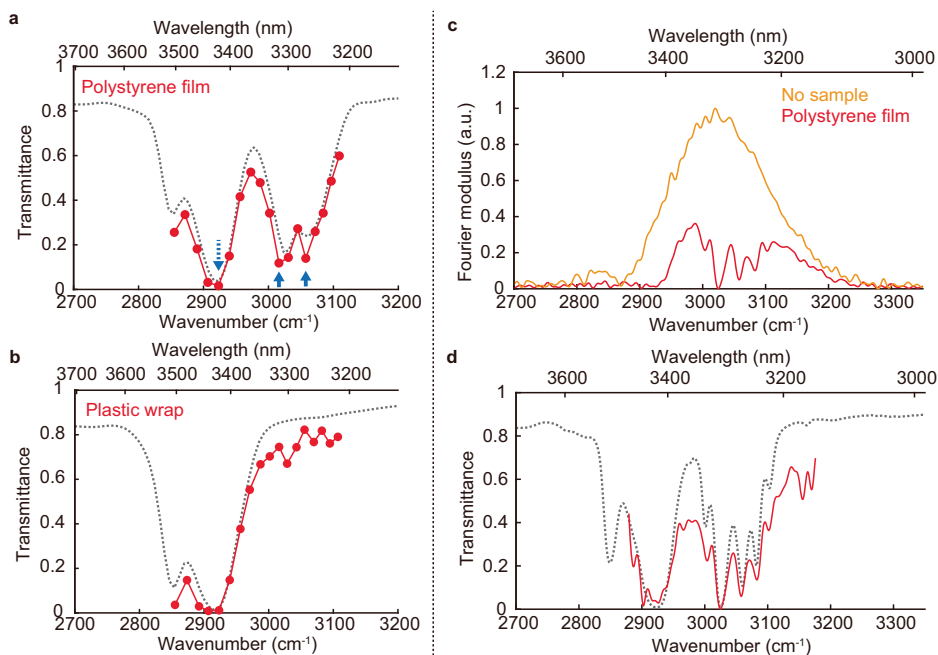
The idler pulse energy in the sample in the ppKTP crystal case is estimated to be ~0.2 pJ (~0.2 nW), while the amplified signal at the interferometer output is 580 pJ (580 nW). The strong parametric amplification allows for non-invasively interrogating a sample with a lower energy idler pulse and detecting the molecular vibration information with a higher energy signal pulse, sufficient for a cost-effective moderate sensitivity detector. In the apKTP crystal case, the signal pulse energy is around 10 pJ (10 nW), corresponding to the photon number per coherence time of ~10^5, being orders of magnitude larger than the low-parametric-gain cases (~10^{-9} and ~10^{-2} in the aperiodically[21] and periodically[20] poled crystal cases, respectively).

The maximum visibility of the signal interferogram is 98%, shown in the inset of Fig. 1. With an idler amplitude transmittance of 0.39, the visibility is 67%, higher than in the low-parametric-gain case (38%). The high-visibility feature allows for sufficiently utilizing the detector's dynamic range when measuring the samples with large absorption.

We evaluate the signal-to-noise ratio (SNR) of the FTIR spectrum measured with our system. The SNR is defined as the ratio of the peak Fourier modulus (signal) of the FTIR spectrum to the standard deviation (noise) where no spectral components exist. In the ppKTP crystal case, the signal and the noise are evaluated at 3107 cm^{-1} and 3303–3717 cm^{-1}, respectively. The SNR of the single-shot 14-cm^{-1}-width FTIR spectrum obtained at a maximum OPD of 1.6 mm and a measurement time of 133 s is 230, corresponding to a minimum transmission change of 1.3% (3σ width). In the apKTP crystal case, the signal and the noise are evaluated at 3020 cm^{-1} and 3462–3763 cm^{-1}, respectively. The SNR of the 36-times averaged 170-cm^{-1}-width FTIR spectrum measured with a maximum OPD of 1.6 mm and a total measurement time of 1581 s is 105, corresponding to a minimum transmission change of 2.9% (3σ width).

We compare the SNR of our system and the low-gain-version FTIR with undetected photons[16] to the best possible accuracy while rigorously comparing two different spectrometers is difficult. The FTIR bandwidth and the resolution of our system with the apKTP crystal are 300 cm^{-1} (170 cm^{-1} at FWHM) and 5 cm^{-1}, respectively, corresponding to the number of spectral elements of 60 (300 cm^{-1}/5 cm^{-1}). The SNR of the 36-times averaged FTIR spectrum is at most 105 with a total measurement time of 1581 s at a detected pulse energy of 10 pJ (mean power of 10 nW). Lindner et al. achieved an SNR of 390 with a spectral bandwidth of 725 cm^{-1}, an apodized-spectral resolution of 1 cm^{-1}, a measurement time of 900 s, and a detected mean power of 20 nW. If the method measures the FTIR spectrum with the same bandwidth,

resolution, measurement time, and mean power as ours, it would have ~40 times better SNR than ours. Note that we assume the SNR is linear in the square root of the measurement time, the square root of the detected power, and the inverse of the number of spectral elements[16]. We also suppose the quantum efficiency and interference contrast are comparable for simplicity.

The difference in SNR originates from the dominant noise difference between our system (relative intensity noise, RIN) and the system developed by Lindner et al. (shot noise). In our system, the noise linearly increases with the signal power on the photodetector (see Supplementary Note 5), i.e., the SNR does not depend on the signal power. We attribute the RIN to the amplification fluctuation and photon thermal statistics, which can be alleviated by stabilizing the pump intensity and increasing the number of spatiotemporal modes, respectively.

Our method can advance with further modifications of the developed system. Using other nonlinear crystals (e.g., AgGaS$_2$ crystal[17,18]), we can also perform FTIR with undetected photons in the molecular fingerprint region. In addition, our system can acquire hyperspectral MIR images[35] by implementing a camera for detection. The principle of this method is also applicable to MIR optical coherence tomography[36,37], which may be useful for the non-invasive 3D imaging of paintings. Furthermore, our method can be integrated into multimodal spectroscopy[38] techniques that also use a pulsed laser to induce multiple nonlinear optical effects at the same time.

Conclusions

In conclusion, we developed a high-parametric-gain SU(1,1) interferometer with ppKTP and apKTP crystals to demonstrate MIR-range FTIR with undetected photons. The FTIR spectra obtained from the interferometer covered up to ~300 cm^{-1} in the 3-μm region. As proof of the principle, we measured the MIR transmittance spectra of polymer films and observed the C–H stretching modes of the molecules. As to the sensitivity, the RIN of the signal pulses limits the SNR, which ineffectively uses a high photon number advantage. Increasing the number of spatiotemporal modes and suppressing the pump intensity fluctuation can improve the SNR of our system in the future.

With the interferometer, we demonstrated strong parametric amplification in the second passage and higher interferometric visibility at a large idler loss, which can be advantageous over low-gain-version FTIR with undetected photons. The amplification enables non-invasive interrogation of a sample with weak idler pulses and detection of the absorption

information through the amplified signal pulses using a photodetector with moderate sensitivity. This significantly unbalanced power makes our method promising for sensing fragile samples—particularly for biological and medical applications. The higher interferometric visibility allows us to use the dynamic range of the detector and the digitizer sufficiently. This feature could be beneficial for measuring target molecules in a significant MIR absorption background, such as water. Furthermore, another merit of our system is that the pump and the twin beams are pulsed. It enables our system to be applied to multimodal nonlinear spectroscopy by simultaneously inducing other nonlinear optical effects with the same pump pulse or time-resolved spectroscopy with the pulsed pump and idler.

Methods
Digitization and post-processing to obtain an FTIR spectrum
The recorded signal interferogram is sampled with an 8-bit digitizer (USB-5133, National Instruments) with a sampling rate of 1.53 k Samples s^{-1}. The interferogram is RF bandpass filtered to remove the DC part and the unwanted high- and low-frequency noises. The OPD of the FTIR interferogram is calibrated with a simultaneously measured continuous-wave interferogram with a helium-neon laser. Fourier-transforming the calibrated FTIR interferogram yields the FTIR spectrum.

Data availability
The data provided in the manuscript are available from the corresponding author upon reasonable request.

Code availability
The Matlab code used to analyze the data of this study are available from the corresponding author upon reasonable request.

References
1. Cossel, K. C. et al. Gas-phase broadband spectroscopy using active sources: progress, status, and applications. *J. Optical Soc. Am. B* **34**, 104–129 (2017).
2. Huber, M. et al. Stability of person-specific blood-based infrared molecular fingerprints opens up prospects for health monitoring. *Nat. Commun.* **12**, 1511 (2021).
3. Griffiths, P. R. & De Haseth, J. A. *Fourier Transform Infrared Spectrometry*. (John Wiley & Sons, Hoboken, 2006).
4. Zheng, T. et al. High-speed mid-infrared single-photon upconversion spectrometer. *Laser Photon Rev.* **17**, 2300149 (2023).
5. Sun, B. et al. Single-photon time-stretch infrared spectroscopy. *Laser Photon. Rev.* https://doi.org/10.1002/lpor.202301272 (2024).
6. Tidemand-Lichtenberg, P., Dam, J. S., Andersen, H. V., Høgstedt, L. & Pedersen, C. Mid-infrared upconversion spectroscopy. *J. Optical Soc. Am. B* **33**, D28 (2016).
7. Neely, T. W., Nugent-Glandorf, L., Adler, F. & Diddams, S. A. Broadband mid-infrared frequency upconversion and spectroscopy with an aperiodically poled LiNbO_3 waveguide. *Opt. Lett.* **37**, 4332–4334 (2012).
8. Hashimoto, K. et al. Upconversion time-stretch infrared spectroscopy. *Light Sci. Appl* **12**, 48 (2023).
9. Kowligy, A. S. et al. Infrared electric field sampled frequency comb spectroscopy. *Sci. Adv.* **5**, eaaw8794 (2019).
10. Pupeza, I. et al. Field-resolved infrared spectroscopy of biological systems. *Nature* **577**, 52–59 (2020).
11. Cai, Y., Chen, Y., Xin, X., Huang, K. & Wu, E. Mid-infrared single-photon upconversion spectroscopy based on temporal-spectral quantum correlation. *Photonics Res.* **10**, 2614–2621 (2022).
12. Cai, Y. et al. Mid-infrared single-photon upconversion spectroscopy enabled by nonlocal wavelength-to-time mapping. *Sci. Adv.* **10**, eadl3503 (2024).
13. Chekhova, M. V. & Ou, Z. Y. Nonlinear interferometers in quantum optics. *Adv. Opt. Photonics* **8**, 104–155 (2016).
14. Kalashnikov, D. A., Paterova, A. V., Kulik, S. P. & Krivitsky, L. A. Infrared spectroscopy with visible light. *Nat. Photonics* **10**, 98–101 (2016).
15. Lindner, C., Wolf, S., Kiessling, J. & Kühnemann, F. Fourier transform infrared spectroscopy with visible light. *Opt. Express* **28**, 4426–4432 (2020).
16. Lindner, C. et al. Nonlinear interferometer for Fourier-transform mid-infrared gas spectroscopy using near-infrared detection. *Opt. Express* **29**, 4035–4047 (2021).
17. Paterova, A. V., Toa, Z. S. D., Yang, H. & Krivitsky, L. A. Broadband Quantum Spectroscopy at the Fingerprint Mid-Infrared Region. *ACS Photonics* **9**, 2151–2159 (2022).
18. Mukai, Y., Okamoto, R. & Takeuchi, S. Quantum Fourier-transform infrared spectroscopy in the fingerprint region. *Opt. Express* **30**, 22624–22636 (2022).
19. Kaufmann, P., Chrzanowski, H. M., Vanselow, A. & Ramelow, S. Mid-IR spectroscopy with NIR grating spectrometers. *Opt. Express* **30**, 5926–5936 (2022).
20. Lindner, C. et al. High-sensitivity quantum sensing with pump-enhanced spontaneous parametric down-conversion. *APL Photonics* **8**, 051301 (2023).
21. Tashima, T. et al. Ultra-broadband quantum infrared spectroscopy. *Optica* **11**, 81–87 (2024).
22. Chekhova, M. V. et al. Broadband bright twin beams and their upconversion. *Opt. Lett.* **43**, 375–378 (2018).
23. Machado, G. J., Frascella, G., Torres, J. P. & Chekhova, M. V. Optical coherence tomography with a nonlinear interferometer in the high parametric gain regime. *Appl Phys. Lett.* **117**, 094002 (2020).
24. Horoshko, D. B. et al. Nonlinear Mach–Zehnder interferometer with ultrabroadband squeezed light. *J. Mod. Opt.* **67**, 41–48 (2020).
25. Sh. Iskhakov, T., Pérez, A. M., Yu. Spasibko, K., Chekhova, M. V. & Leuchs, G. Superbunched bright squeezed vacuum state. *Opt. Lett.* **37**, 1919–1921 (2012).
26. Hashimoto, K., Horoshko, D. B. & Chekhova, M. V. Broadband spectroscopy and interferometry with undetected photons at strong parametric amplification. *Adv. Quantum Technol*. https://doi.org/10.1002/qute.202300299 (2023).
27. Jacco, J. C. & Loiacono, G. M. Nature of the infrared spectrum in band-edge region of KTiOPO4. *Appl. Phys. Lett.* **58**, 560–561 (1991).
28. Flórez, J., Lundeen, J. S. & Chekhova, M. V. Pump depletion in parametric down-conversion with low pump energies. *Opt. Lett.* **45**, 4264–4267 (2020).
29. Horoshko, D. B. & Kolobov, M. I. Towards single-cycle squeezing in chirped quasi-phase-matched optical parametric down-conversion. *Phys. Rev. A* **88**, 033806 (2013).
30. Horoshko, D. B. & Kolobov, M. I. Generation of monocycle squeezed light in chirped quasi-phase-matched nonlinear crystals. *Phys. Rev. A* **95**, 033837 (2017).
31. Boulanger, B. et al. Optical studies of laser-induced gray-tracking in KTP. *IEEE J. Quantum Electron* **35**, 281–286 (1999).
32. Narayana Perumal, R., Nallathambi, A. & Subramani, S. Review on gray track effects on potassium titanyl phosphate single crystals. *Juniper Online J. Mater. Sci.* **3**, 555612 (2017).
33. Kaur, J., Mukai, Y., Okamoto, R. & Takeuchi, S. Spectral domain nonlinear quantum interferometry with pulsed laser excitation. *Phys. Rev. A* **108**, 063714 (2023).
34. Smith, B. C. The infrared spectra of polymers III: hydrocarbon polymers. *Spectroscopy* https://doi.org/10.56530/spectroscopy.mh7872q7 (2021).
35. Paterova, A. V., Maniam, S. M., Yang, H., Grenci, G. & Krivitsky, L. A. Hyperspectral infrared microscopy with visible light. *Sci. Adv.* **6**, eabd0460 (2020).

36. Paterova, A. V., Yang, H., An, C., Kalashnikov, D. A. & Krivitsky, L. A. Tunable optical coherence tomography in the infrared range using visible photons. *Quantum Sci. Technol.* **3**, 025008 (2018).
37. Vanselow, A. et al. Frequency-domain optical coherence tomography with undetected mid-infrared photons. *Optica* **7**, 1729–1736 (2020).
38. Sinjab, F., Hashimoto, K., Badarla, V. R., Omachi, J. & Ideguchi, T. Multimodal laser-scanning nonlinear optical microscope with a rapid broadband Fourier-transform coherent Raman modality. *Opt. Express* **28**, 20794–20807 (2020).

Author contributions
M. V. C. conceived the concept of this study. K.H. designed and built the optical setup. D. B. H. and M. I. K. designed the nonlinear crystal based on theoretical calculations. Y. M. and Z. G. fabricated the nonlinear crystals. K.H. performed the experiments and analyzed the data. D. B. H. and M. I. K. theoretically interpreted the results. M. V. C. supervised the entire work. K.H. wrote the paper with the support of M. V. C. and D. B. H. and all authors contributed to improving the paper.

Competing interests
The authors declare no competing interests.

Additional information
Supplementary information The online version contains supplementary material available at https://doi.org/10.1038/s42005-024-01717-3.

Correspondence and requests for materials should be addressed to Kazuki Hashimoto.

Peer review information *Communications Physics* thanks the anonymous reviewers for their contribution to the peer review of this work.

Reprints and permissions information is available at http://www.nature.com/reprints

Publisher's note Springer Nature remains neutral with regard to jurisdictional claims in published maps and institutional affiliations.